Rock Mech. Rock Engng. (2007) 40 (1), 41–61
DOI 10.1007/s00603-006-0081-z
Printed in The Netherlands

Rock Mechanics and Rock Engineering

The Hydro-Mechanically Coupled Response of Rock Fractures

By

G. Cammarata[1], **C. Fidelibus**[2], **M. Cravero**[3], and **G. Barla**[1]

[1] Department of Structural and Geotechnical Engineering, Politecnico di Torino, Turin, Italy
[2] Department of Earth Sciences, Swiss Federal Institute of Technology (ETH), Zürich, Switzerland
[3] Institute of Environmental Geology and Geoengineering, National Research Council, Turin, Italy

Received September 8, 2005; accepted January 20, 2006
Published online March 27, 2006

Summary

In a fractured rock mass, variations in stress and fluid pressure induced by engineering activities can significantly affect the hydrogeological properties. A significant change in fracture transmissivities can also be experienced in the far-field. The simulation of this kind of change requires a Hydro-Mechanical (HM) coupled model. The purpose of this paper is to show how such a model can be used to analyse the evolution of deformation and pressure in a fracture subjected to fluid injection. A 2D BEM-FEM code is used to solve the non-linear system of equations that describe the dependency of transmissivity on local fracture closure. The results of a sensitivity analysis of the essential fracture parameters allow one to gain insight into the importance of the HM models in the framework of the hydrogeology of fractured rock masses. Results obtained from a system of two impervious blocks and a saturated fracture are reported, in order to show the possibilities offered by this technique.

Keywords: BEM-FEM code; fractured rock hydrogeology, hydro-mechanical (HM) coupling.

1. Introduction

Theoretical and experimental studies on Hydro-Mechanical (HM) coupling in rock masses have been performed over the last two decades. At present there is widespread interest in the implications of HM coupling for several engineering applications in the field of fractured rock hydrogeology. Furthermore, many geological processes can only be reasonably predicted if a HM coupling is also considered.

Wang (2000) made a distinction between *direct* and *indirect* HM coupling. In the first case, the coupling implies variations in the field variables (stress and pressure) of

the system, without any modification of its mechanical properties. In the second case, a reduction in the pore or fracture volume results in a stiffer and less permeable material. Indirect HM coupling is predominantly used in fractured rock; under the variation of stress, fracture transmissivity can drastically change and significantly affect the flow regime.

When indirect HM coupling takes place, the use of a numerical technique, which accounts for these mechanical and hydrogeological changes, is therefore essential for an appropriate prediction of the fluid flow, in particular when dealing with near-field problems.

A computer code has been developed to simulate the transient fluid flow in a discrete assembly of rock blocks and percolative fractures. This new development is based on a procedure that has been set up and implemented at the Department of Earth Sciences of the ETH (Fidelibus, 2003).

The local stress balance equations for the blocks are numerically solved using a direct formulation of the Boundary Element Method (BEM), whereas the diffusion equation in the fractures is dealt with using the Finite Element Method (FEM) and a Galerkin weighted residual procedure. Finally, the equations that describe the mechanical behaviour of the fracture are directly rendered in algebraic form.

This paper provides an overview of the influence of fracture deformability on the transient flow response of a fracture. A system of two impervious blocks and a saturated fracture is considered. The numerical results of a sensitivity analysis of the fracture properties highlight the importance of HM coupling in the study of the behaviour of fractured rocks.

2. Governing Equations

As previously mentioned, BEM integral equations are used to solve the local stress balance equations of the blocks. Several advantages can be obtained when using BEM:

1. In the absence of body forces, the method provides a reduction in the dimensionality of the problem, by transforming the governing equations into an integral exact-form in terms of only the relevant quantities at the boundaries.
2. In a rather irregular system of fractures and porous blocks, only the discretization of the lines that represent the fractures is needed.
3. The results do not improve consistently if the discretization is performed by dividing the boundary segments into elements of different sizes; for this reason it is reasonable to divide each boundary linear-segment into equal-sized elements. As a consequence, the pre-processing is fast, and the results are more readable, as they only refer to fractures or blocks boundary points and external boundaries.

If a discrete model is assumed under isothermal conditions, the simulation of the fluid flow and deformation of a fractured medium only requires the specializing of the local stress balance equations for both blocks and fractures and fluid continuity equations for fractures. A specific traction versus relative displacement relation for the fractures is also needed. The governing equations are given in what follows.

2.1 Deformable Impervious Blocks

According to a reference system of global coordinates $\mathbf{x}$, for a domain Ω composed of a linear elastic and impervious material bounded by Γ, if the inertial effects are neglected, the local stress balance equations can be written as follows:

$$\sigma_{ij,i} + f_j = 0, \tag{1}$$

where σ_{ij} is the total stress tensor and f_j are the body forces per unit volume.

The stress can be expressed as:

$$\sigma_{ij} = \sigma_{ij}^0 + \Delta\sigma_{ij}, \tag{2}$$

where σ_{ij}^0 is the initial state of stress and $\Delta\sigma_{ij}$ the stress increment. Let us assume that both body forces and initial stresses are zero. As a consequence $\sigma_{ij} = \Delta\sigma_{ij}$, which holds for the following.

The Hooke stress-strain equation applies:

$$\sigma_{ij} = 2G\epsilon_{ij} + \lambda\epsilon_{\text{vol}}\delta_{ij}, \tag{3}$$

where G and λ are the Lamé constants, ϵ_{ij} the strain tensor, ϵ_{vol} the volumetric strain and δ_{ij} the Kroenecker delta. The σ_{ii} stresses are positive when they stretch the material.

Given the hypothesis of small displacements, the following equation applies:

$$\epsilon_{ij} = \frac{1}{2}(u_{i,j} + u_{j,i}), \tag{4}$$

where u_i are the displacements.

By inserting Eqs. (3) and (4) into Eq. (1) with $f_j = 0$ and given $\epsilon_{\text{vol}} = \epsilon_{kk}$, the following Navier equation can be derived:

$$(\lambda + G)\frac{\partial^2 u_j}{\partial x_i \partial x_j} + G\frac{\partial^2 u_i}{\partial {x_j}^2} = 0. \tag{5}$$

2.2 Deformable and Percolative Fractures

The percolation model for a planar, rough, deformable fracture requires significant simplifications in order to be conveniently reduced to a 2D scheme. As a consequence of the effective stress variation, the model has to account for the deformations of fracture contacts, which implies a variation of the void volume and transmissivity of the fracture. The model has to be geometrically and mechanically characterized.

With reference to a local coordinate system $\mathbf{x}'$, with x_1', x_3' in the mean plane of the fracture and x_1' parallel to the flow direction, the geometrical characterization of a conductive section (x_2', x_3' plane) of width w requires a simplified representation of the real roughness profile of the fracture walls where the morphology is sampled by n_t intervals, each Δw long, while in the flow direction x_1', the fracture is divided into elements of length L^i (Figs. 1 to 3).

This L^i value should be less than the spatial correlation length l_c for the apertures, i.e. the distance within which the aperture values along the direction of the flow are closely correlated to each other. The spatial correlation structure of apertures has been evaluated in fractures that have to be submitted to fluid flow tests under normal

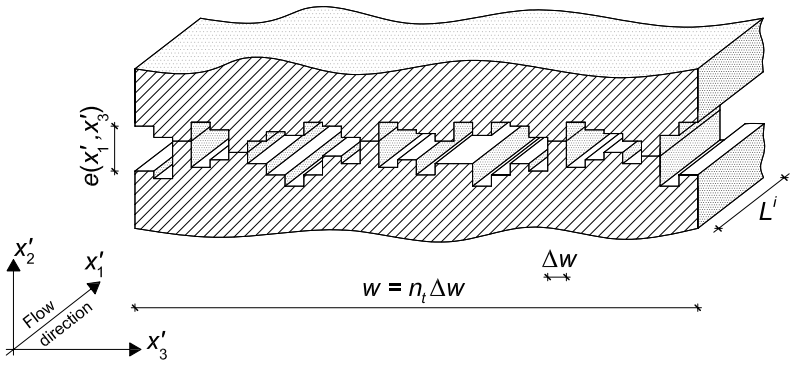

Fig. 1. Idealized model of the fracture

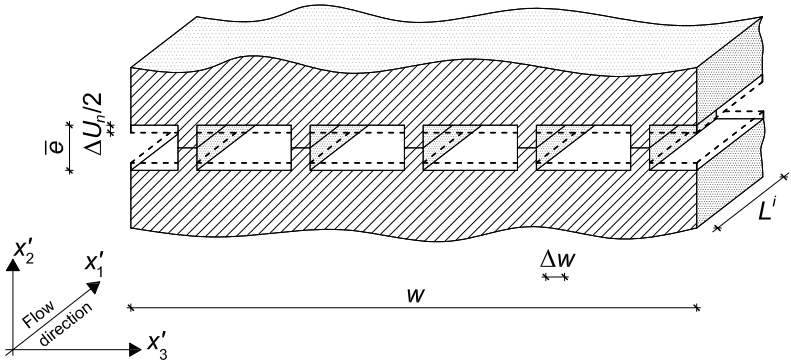

Fig. 2. Regular arrangement of the void volume and contacts

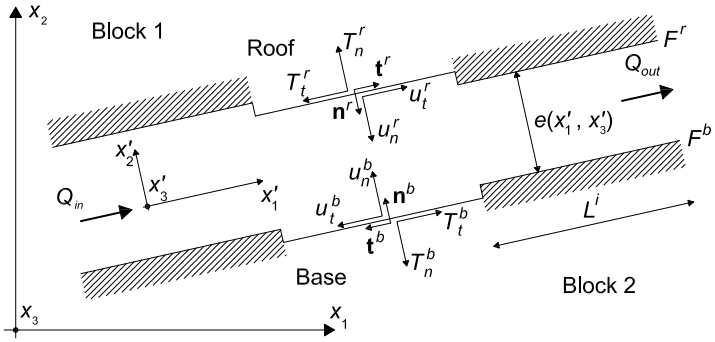

Fig. 3. Coordinate system for a fracture of an arbitrary orientation

(Hakami, 1995) and shear displacement (Yeo et al., 1998) conditions. The estimated l_c ranges from 10–20 mm for well matched fractures of up to 5–10 cm for the faults. Provided the differences in the aperture values within l_c are small, the assumption of

constant aperture within L^i is an acceptable approximation. This model is similar to the one that has recently been proposed by McDermott and Kolditz (2004).

For a given stress level, the void volume V_v^i of a fracture element of length L^i and width w is in general as follows:

$$V_v^i = \int_0^{L^i} \int_0^w e(x_1', x_3') dx_1' dx_3', \tag{6}$$

where a local aperture distribution $e(x_1', x_3')$ is introduced. If the idealization of Fig. 1 is considered and provided that, for a specific interval j, the aperture assumes a constant value e^j along x_1', Eq. (6) can be modified as follows:

$$V_v^i = L^i \sum_{j=1}^{n_v} (\Delta w e^j) = L^i n_v \Delta w \bar{e} = L^i (1-d) w \bar{e}, \tag{7}$$

where n_v is the number of intervals with not zero aperture, $\bar{e}$ is the average aperture value within the element and $d = (n_t - n_v)/n_t$ is the ratio of the contact area of the asperities to the total fracture area.

The introduction of the average aperture allows the fracture to be idealized as a regular array of voids with length $(1-d)w/(n_t - n_v)$ and height $\bar{e}$ (Fig. 2).

The average aperture $\bar{e}$ is therefore:

$$\bar{e} = \frac{\sum_{j=1}^{n_v} (\Delta w e^j)}{(1-d)w}, \tag{8}$$

which is tendentially close to the estimate of the aperture $E(e)$ which is equal to the mean value of the distribution $f(e)$:

$$E(e) = \int_0^\infty e f(e) de. \tag{9}$$

Changes in the normal stress level determine a variation in the void volume ΔV_v^i, which can be written as follows:

$$\Delta V_v^i = L^i w \Delta[(1-d)\bar{e}] \cong L^i w (1-d) \Delta \bar{e}, \tag{10}$$

provided $(1-d)$ is constant in the idealized model.

A traction-relative displacement relationship of the fracture walls is necessary in order to relate ΔV_v to the fracture deformation:

$$\begin{pmatrix} T_n + p \\ T_t \end{pmatrix} = \begin{pmatrix} -k_{nn} & k_{nt} \\ k_{tn} & -k_{tt} \end{pmatrix} \begin{pmatrix} U_n \\ U_t \end{pmatrix}, \tag{11}$$

where, with reference to Fig. 3, T_n and T_t are the normal and shear tractions (stress vector components), p is the water pressure ($T_n + p = T_n'$ is the effective stress), U_n (*fracture closure*) and U_t are the normal and shear relative displacement components equal to $u_n^r + u_n^b$, $u_t^r + u_t^b$, respectively, and k_{nn}, k_{tt}, k_{nt} and k_{tn} are the fracture stiffness components that are closure-dependent. The fracture wall displacements are positive, conforming to the positive signs of $\mathbf{n}^r$, $\mathbf{n}^b$, $\mathbf{t}^r$, $\mathbf{t}^b$. The minus sign of the diagonal stiffness coefficients derives from the convention that was introduced, where T_n are positive when they tend to open the fracture and T_t are positive when a couple tends to spin the fracture in the anti-clockwise direction.

Based on the model in Fig. 2, the variation in fracture closure is equal to minus the variation of the average aperture ($\Delta U_n = -\Delta\bar{e}$). This simple position synthesizes the HM coupling for a percolative and deformable fracture. A reduction (or increase) in void space, driven by an external load or pore pressure perturbation, in turn affects the amount of water that is stored in the fracture (direct coupling) and, as later described through the introduction of the cubic law, the transmissivity (indirect coupling).

Given this theoretical framework, there is no need to utilize the concept of *mechanical aperture* e_m. However, one can take the mechanical aperture to be equal to the average aperture and assume that:

$$e_m = e_{m0} - \Delta U_n = e_{m0} + \Delta\bar{e}, \tag{12}$$

where e_{m0} is an initial value that is related to the initial stress state.

Once the variation of the average aperture $\Delta\bar{e}$ in Eq. (10) is replaced by the variation in fracture closure ΔU_n, one obtains:

$$\Delta V_v^i = -L^i w(1-d)\Delta U_n. \tag{13}$$

However, this model does not explicitly take into account the actual phenomena (i.e.: local variations of fracture closure, lateral deformation or crushing of contacting asperities and new contact formation) that occur in the fracture zone, during the loading process. Some discrepancy occurs, due to these phenomena, between the computed ΔU_n and the measured apparent closure ΔU_n^* of the fracture zone during loading tests on rock samples.

A more general expression should be given as follows:

$$\Delta V_v^i = -L^i w\Delta(f_c U_n), \tag{14}$$

where a stress-dependent coefficient f_c is introduced which implicity accounts for the relationship between the computed and measured apparent closure, and for the nonlinear variation of d.

An averaging operation is also necessary to describe the variation in the fluid discharge along the flow direction x_1' (Fig. 3). Namely, in a given time interval Δt, the water mass balance of the element L^i of the saturated fracture ($V_v = V_w$) has to be written as:

$$\left[\int_{F^{b,i}}^{F^{r,i}} \rho_w q_{x_1'}\left(x_1' + \frac{L^i}{2}, x_2', t\right)dx_2' - \int_{F^{b,i}}^{F^{r,i}} \rho_w q_{x_1'}\left(x_1' + \frac{L^i}{2}, x_2', t\right)dx_2'\right] w\Delta t$$
$$= -\Delta M_w^i = M_w(x_1', t) - M_w(x_1', t+\Delta t), \tag{15}$$

where $q_{x_1'}$ is the specific discharge (i.e. the average water velocity normal to a given conductive section), ρ_w is the water density, the functions F^r and F^b represent the fracture walls (*roof* and *base* respectively) and ΔM_w^i is the mass of water stored in or released by the fracture.

The variation in the mass of water ΔM_w^i is expressed as follows:

$$\Delta M_w^i = \Delta(\rho_w V_w) = V_w\Delta\rho_w + \rho_w\Delta V_w, \tag{16}$$

where the indication of the element i is omitted; Equation (16), according to Eqs. (7) and (14) and assuming $w = 1$, can be written as:

$$\Delta M_w^i = L^i[(1-d)\bar{e}\Delta\rho_w - \rho_w\Delta(f_c U_n)]. \tag{17}$$

It is worth noticing that the previously introduced coefficient f_c acts as a *coupling factor*, relating the volume of water released (or stored) in the fracture per unit length of the fracture to the increase (or reduction) of the fracture closure.

By assuming that the density of water does not vary in the x_2' direction ($\rho_w = \rho_w(x_1', t)$), it is possible to write:

$$\int_{F^b(x_1')}^{F^r(x_1')} \rho_w(x_1', t) q_{x_1'}(x_1', x_2', t) dx_2' = \rho_w Q_{x_1'}(x_1', t), \tag{18}$$

where $Q_{x_1'}$ is the discharge per unit width.

By inserting Eqs. (17) and (18) into Eq. (15), the latter is modified as follows:

$$\left[\rho_w Q_{x_1'}\left(x_1' + \frac{\Delta x_1'}{2}, t\right) - \rho_w Q_{x_1'}\left(x_1' - \frac{\Delta x_1'}{2}, t\right)\right]\Delta t = -\Delta x_1'[(1-d)\bar{e}\Delta\rho_w - \rho_w \Delta(f_c U_n)], \tag{19}$$

where $\Delta x_1' = L^i$ and all the quantities on the right hand side refer to the element centered in x_1'. This equation still refers to an element of the idealized section of Fig. 3, where teeth-like surfaces bound the void space; this would give rise to a solution scheme where each element is equivalent to a *resistor* of given properties. However, in order to give more generality to the code, a partial differential equation is derived by letting Δt, $\Delta x_1' \to 0$:

$$\frac{\partial(\rho_w Q_{x_1'})}{\partial x_1'} + (1-d)\bar{e}\frac{\partial \rho_w}{\partial t} - \rho_w \frac{\partial(f_c U_n)}{\partial t} = 0. \tag{20}$$

By developing the partial derivatives of the excess of the mass discharge and of the fracture closure with time one obtains:

$$\rho_w \frac{\partial Q_{x_1'}}{\partial x_1'} + Q_{x_1'}\frac{\partial \rho_w}{\partial x_1'} + (1-d)\bar{e}\frac{\partial \rho_w}{\partial t} - \rho_w f_c \frac{\partial U_n}{\partial t} - \rho_w U_n \frac{\partial f_c}{\partial t} = 0. \tag{21}$$

Let us assume that the spatial variations in ρ_w are much smaller than the local, temporal ones (grad$\rho \ll \partial\rho/\partial t$) (Bear, 1979), and that the temporal variations of f_c are much smaller than those of U_n, in such a way the second and the last terms of Eq. (21) are negligible:

$$\rho_w \frac{\partial Q_{x_1'}}{\partial x_1'} + (1-d)\bar{e}\frac{\partial \rho_w}{\partial t} - \rho_w f_c \frac{\partial U_n}{\partial t} = 0. \tag{22}$$

The state of the fluid equation (the relationship between the density and the pressure) is as follows:

$$\rho_w = \rho_{w,0} e^{\beta_w (p - p_0)}, \tag{23}$$

where β_w is the fluid (water) compressibility and $\rho_{w,0}$ the reference value for the water density at the reference pressure p_0. By differentiating, with respect to p, the temporal derivative of p can be replaced. It follows that:

$$\frac{\partial Q_{x_1'}}{\partial x_1'} + \beta_w (1-d)\bar{e}\frac{\partial p}{\partial t} - f_c \frac{\partial U_n}{\partial t} = 0, \tag{24}$$

where ρ_w has been removed.

In analogy with the *generalized Darcy law* (Bear and Bachmat, 1990), a general expression for the fluid discharge can be introduced:

$$Q_{x'_1} = -\frac{T_f}{\rho_w|\mathbf{g}|}\left(\frac{\partial p}{\partial x'_1} - \rho_w g_{x'_1}\right) = -\frac{T_f}{\rho_w|\mathbf{g}|}\frac{\partial P}{\partial x'_1}, \tag{25}$$

where the reduced pressure $P = p + \rho_w|\mathbf{g}|z$ is included and T_f is the fracture transmissivity which in this work is evaluated by means of the *cubic law*:

$$T_f = \frac{g e_h^3}{12\nu_w}, \tag{26}$$

where the *hydraulic aperture* e_h is introduced and ν_w is the kinematic viscosity. Since this law defines a representative distance between two smooth, parallel fracture walls, the following relation holds for the idealized adopted model (Fig. 2):

$$e_h = \bar{e}(1-d). \tag{27}$$

Taking this relation and Eq. (12) into consideration, the following can be written:

$$\Delta e_h = (1-d)\Delta e_m \tag{28}$$

or, in more general form:

$$\Delta e_h = f_c \Delta e_m, \tag{29}$$

with f_c again being stress-dependent.

Cornet et al. (2003) investigated this relation through a field experiment on a single fracture subject to flow injection but with a couple of flat jacks controlling the normal stress. They noticed that a non-linear relation holds for a sequence of increasing injection pressures, with two distinct phases. In the first phase, the opening of the fracture does not affect the transmissivity and low flow rates occur. Then, when a certain critical value is reached, an equal increase in the mechanical aperture occurs for an increase in the hydraulic aperture. This is consistent with a lack of contact and $d = 0$ in Eq. (28).

Substituting Eqs. (25) and (27) in Eq. (24) yields the final expression of the continuity equation which is given by:

$$\frac{1}{\rho_w|\mathbf{g}|}\frac{\partial}{\partial x'_1}\left(T_f\frac{\partial P}{\partial x'_1}\right) = \beta_w\frac{\partial P}{\partial t}e_h - f_c\frac{\partial U_n}{\partial t}. \tag{30}$$

One can observe that the flow regime through a fracture is essentially complex: for instance, as observed by Yeo et al. (1998), shear deformation introduces flow heterogeneities and the 1D scheme here adopted could be too simplifying.

If the right-hand side of Eq. (30) is set to zero (steady-state flow), it can be written as follows:

$$\frac{d}{dx'_1}\left(e_h^3\frac{dP}{dx'_1}\right) = 0, \tag{31}$$

which is the Reynolds lubrication-type flow equation. This equation is an approximation of the Navier-Stokes equations for an incompressible viscous fluid flowing in a void space limited by rough surfaces and *non-slip* conditions between the fluid and

solid. This equation has also been derived by assuming the cubic law to be valid locally.

The validity of Eq. (31) is ensured if the aperture is much less than a characteristic length λ_w along x_1', defined as a distance within which the apertures do not vary consistently and can be assimilated to the spatial correlation length l_c. If this condition does not hold, the discrepancy between the (true) solution of the Navier-Stokes equations and the solution provided by Eq. (31) can be consistent. Furthermore, if the flowrate is not sufficiently small, the relation between the discharge and the pressure gradient can be non-linear, even before the threshold that marks the transition from laminar to turbulent flow is reached.

Zimmerman and Bodvarsson (1996) defined the transition limit between the linear and non-linear phases as follows:

$$\frac{dP}{dx_1'} = \frac{12\rho\nu_w^2}{e^4}. \tag{32}$$

The reduced pressure gradient value is probably almost always exceeded in the near-field of well injections.

3. The Numerical Scheme

A computer code (POSEIDON[1]) has been developed based on the previous equations. It utilizes the direct Boundary Element Method (BEM) for the discretization, in space, of Eq. (5) for the blocks of the system, while a Finite Element Method (FEM) representation with a Galerkin weighted residual procedure is used for the fracture Eq. (30), with temporal derivatives rendered in finite differences. Finally, Eq. (11) is explicitly written and included in the equation system. The time interval is divided into time steps of constant duration and all the variables are constant within a single step. The spatial discretization is limited to only the fractures. The variables are constant along a single element, except for the pressure, whose representation is quadratic (three nodes per element).

3.1 BEM Integral Equations

The Boundary Element Method equation for elastostatics (Brebbia et al., 1984; Becker, 1992) derives from the application of the Somigliana identity and the use of the fundamental solutions of Eq. (5). It follows that:

$$c_{ij}u_j(\mathbf{x}_c) = \int_\Gamma u_{ij}^*(\mathbf{x}_c, \mathbf{x})T_j(\mathbf{x})d\Gamma(\mathbf{x}) - \int_\Gamma T_{ij}^*(\mathbf{x}_c, \mathbf{x})u_j(\mathbf{x})d\Gamma(\mathbf{x}), \tag{33}$$

where c_{ij} – called the free term – is a geometrical factor; $\mathbf{u}$ and $\mathbf{T}$ are the unknown displacements and tractions in a domain Ω with boundary Γ; $\mathbf{u}^*$ and $\mathbf{T}^*$ are the Kelvin fundamental solutions of Eq. (5), given for an infinite domain Ω^*, made up of the same material as the body under consideration, when a concentrated unit load applies in a collocation node $\mathbf{x}_c$.

[1] POSEIDON (POro-SEctIoned medium DeformatiON analysis)

In 2D plane-strain problems, the fundamental solutions are as follows:

$$u_{ij}^{*}(\mathbf{x}_c, \mathbf{x}) = \frac{\chi}{2G}[(3 - 4\nu_r)\ln(r)\delta_{ij} - r_{,i}r_{,j}] \tag{34}$$

$$T_{ij}^{*}(\mathbf{x}_c, \mathbf{x}) = \frac{\chi}{r}\left\{[(1 - 2\nu_r)\delta_{ij} + 2r_{,i}r_{,j}]\frac{\partial r}{\partial n} - (1 - 2\nu_r)(r_{,i}n_j - r_{,j}n_i)\right\}, \tag{35}$$

where ν_r is the Poisson ratio of the rock blocks, $r = r(\mathbf{x}_c, \mathbf{x})$ represents the distance between the collocation point $\mathbf{x}_c$ and the field point $\mathbf{x}$, $\chi = -[4\pi(1 - \nu_r)]^{-1}$ and n is the normal at the boundary in $\mathbf{x}$.

Each segment of the periphery of a block Ω bounded by Γ is discretized in equal-length elements. The centroid of a generic element hosts the displacements $\mathbf{u}$ and tractions $\mathbf{T}$ as primary unknowns; these unknowns are constant within each element.

If a collocation point is located in each node i of the discretization, a set of integral equations is derived by re-arranging Eq. (33) as follows:

$$\mathbf{c}(\mathbf{x}_i) + \sum_{j=1}^{n_e}\int_{\Gamma_i}\mathbf{T}^{*}(\mathbf{x}_i, \mathbf{x}_j)\mathbf{u}(\mathbf{x}_j)d\Gamma_j - \sum_{j=1}^{n_e}\int_{\Gamma_j}\mathbf{u}^{*}(\mathbf{x}_i, \mathbf{x}_j)\mathbf{T}(\mathbf{x}_j)d\Gamma_j = 0, \tag{36}$$

where $\mathbf{u}(\mathbf{x}_j)$ and $\mathbf{T}(\mathbf{x}_j)$ are the nodal displacements and tractions in the element j whose centroid has coordinates $\mathbf{x}_j$. If $n_e(i_b)$ is the number of elements of a block i_b, $2n_e(i_b)$ new equations can be introduced.

Given n_b blocks, $2n_e(i_b) \times n_b$ BEM equations are available, while $4n_e(i_b) \times n_b$ are the introduced unknowns. For all the blocks, it follows that:

$$\mathbf{A}\mathbf{u}^{\Lambda} + \mathbf{B}\mathbf{T}^{\Lambda} = 0, \tag{37}$$

where $\mathbf{A}$ and $\mathbf{B}$ are matrices of coefficients, produced through the numerical solution of the integrals in Eq. (36). The apex Λ refers to the solution at time step $\Lambda\Delta t$. It should be noted that $\mathbf{A}$ and $\mathbf{B}$ are calculated and stored at the beginning of the process and retrieved at each time step.

3.2 FEM Equations of the Diffusion in the Fracture Network

The discretization of the fractures using 1D elements is consistent with that performed along the block boundaries. This 1D scheme makes a fracture geometrically coincident with the faces of the opposing blocks that contain the fracture. The centroids of the elements that make up the fractures coincide with the centroids of the discretization elements of the opposing rock blocks. The tractions and displacements are constant in each element, while pressure has a quadratic distribution. Aperture e_h is also constant within each element, consistent with the hypothesis in Section 2.2. Uniform tractions and displacements do not require the treatment of discontinuities at the corners of the blocks. A similar scheme with shape functions that were differentiated for the unknowns were used in a previous paper (Fidelibus et al., 1997).

The application of a Galerkin weighted residual procedure leads to the following integral FEM expression of Eq. (30) written for each node i of a fracture of lenght L:

$$-\int_L \frac{T_f}{\rho_w|\mathbf{g}|}\frac{dN_i}{dx_1'}\frac{dN_j}{dx_1'}p_j dx_1' = \int_L \beta_w e_h N_i N_j \frac{dp_j}{dt}dx_1' - \int_L f_c N_i \frac{dU_n}{dt}dx_1', \tag{38}$$

where $p = N_j p_j$, with N_j the shape functions.

The integrals in Eq. (38) are equal to the summation of the integrals computed for each element k that makes up the fracture. For a network of n_f fractures, the spatial discretization leads to the following system of first-order differential equations:

$$-\frac{1}{\rho_w|\mathbf{g}|}\sum_{k=1}^{n_e} T_f^k \mathbf{C}^k \mathbf{p} = \beta_w \sum_{k=1}^{n_e} e_h^k \mathbf{E}^k \dot{\mathbf{p}} - \sum_{k=1}^{n_e} f_c^k \mathbf{D}^k \dot{\mathbf{U}}_\mathbf{n}, \tag{39}$$

where n_e is the total number of elements in the network and $\mathbf{C}^k$, $\mathbf{D}^k$ and $\mathbf{E}^k$ are element matrices, that are expressed as follows:

$$C_{ij}^k = \int_{L^k} \frac{dN_i dN_j}{dx_1' dx_1'} dx_1' = \frac{1}{|\mathbf{J}|}\int_{-1}^{+1} \frac{dN_i dN_j}{d\xi d\xi} d\xi \tag{40}$$

$$D_i^k = \int_{L^k} N_i dx_1' = |\mathbf{J}| \int_{-1}^{+1} N_i d\xi \tag{41}$$

$$E_{ij}^k = \int_{L^k} N_i N_j dx_1' = |\mathbf{J}| \int_{-1}^{+1} N_i N_j d\xi, \tag{42}$$

where i and j range from 1 to n_n, that is, the number of fracture nodes in the network. In the above expressions, the adimensionalized coordinate ξ and the Jacobian $|\mathbf{J}| = L^k/2$ are introduced, with L^k being the length of the element k.

Given the subdivision into a number of equal time increments, with reference to a time station $\Lambda\Delta t$, the time derivatives in Eq. (39) are discretized by the finite difference approximation using a fully implicit scheme:

$$\left(\frac{dp_j}{dt}\right)^\Lambda = \frac{p_j^\Lambda - p_j^{\Lambda-1}}{\Delta t} \tag{43}$$

$$\left(\frac{dU_n}{dt}\right)^\Lambda = \frac{U_n^\Lambda - U_n^{\Lambda-1}}{\Delta t}. \tag{44}$$

Substituting Eqs. (43) and (44) in Eq. (39), after rearranging the terms so that the unknowns appear on the left-hand side and the known quantities on the right-hand side, the following algebraic expression is derived:

$$\begin{aligned} &-\frac{1}{\rho_w|\mathbf{g}|}\sum_{k=1}^{n_e} T_f^k \mathbf{C}^k \mathbf{p}^\Lambda - \frac{\beta_w}{\Delta t}\sum_{k=1}^{n_e} e_h^k \mathbf{E}^k \mathbf{p}^\Lambda + \frac{1}{\Delta t}\sum_{k=1}^{n_e} f_c^k \mathbf{D}^k \mathbf{U}_n^\Lambda \\ &\quad = \frac{\beta_w}{\Delta t}\sum_{k=1}^{n_e} e_h^k \mathbf{E}^k \mathbf{p}^{\Lambda-1} + \frac{1}{\Delta t}\sum_{k=1}^{n_e} f_c^k \mathbf{D}^k \mathbf{U}_n^{\Lambda-1}. \end{aligned} \tag{45}$$

3.3 Traction-relative Displacement Equations

Equation (11) can be written for the centroid of a generic element i in compact form as follows:

$$\begin{pmatrix} T_n^{i\Lambda} + \overline{p}^{i\Lambda} \\ T_i^{i\Lambda} \end{pmatrix} = \mathbf{k}_{\text{sec}}^i \begin{pmatrix} U_n^{i\Lambda} \\ U_i^{i\Lambda} \end{pmatrix}, \tag{46}$$

where a secant stiffness matrix $\mathbf{k}^i_{\text{sec}}$ is introduced (see Section 4.2) and $\overline{p^i}$ is the average water pressure evaluated by interpolating the nodal pressures p_1, p_2, p_3 along the element i through the shape functions N_1, N_2, N_3:

$$\overline{p^i} = \frac{\int_{L^i} N_j(x'_1) p_j dx'_1}{L^i} = \frac{1}{6}p_1 + \frac{2}{3}p_2 + \frac{1}{6}p_3. \tag{47}$$

Equations (37), (45) and (46) form a non-linear system where $\mathbf{k}^i_{\text{sec}}$ is stress-dependent, while T_f, e_h and f_c depend on the displacements of the fracture walls. This system can be solved by the iterative Picard method (Huyakorn and Pinder, 1983).

4. HM Response of a Single Fracture

As already discussed, several engineering activities can modify the flow regime in a fractured rock mass. In particular conditions, the fracture deformation affects the hydrogeological properties of the rock-fracture system. As a consequence, a hydro-mechanically coupled model is needed to better capture the transient evolution of the pressure and discharges. Uncoupled models are not in fact appropriate for the simulation of the transient phenomenon. The use of these models is only justified when the local variations of transmissivity are negligible and, in addition, the total isotropic stress can be reckoned to be constant in time.

In the following, the results of a simulation of a plane fluid flow in a deformable fracture subjected to fluid injection under constant head are given. The purpose of this simulation is to underline the importance of coupled processes in the flow through fractured rock masses and to show the suitability of the implemented numerical algorithms to cope with such a problem.

The authors are aware that the assumption of plane flow (and plane strain) is not realistic when dealing with borehole injection tests in single fractures. For several reasons the use of an axis-symmetric model is also not fully appropriate and only a three-dimensional model can depict the flow regime and the strain/stress field in the rock mass. A two-dimensional scheme is justified here as it is only used to illustrate the effects of the HM coupling. However, the extension of this study to three-dimensional conditions is necessary.

The case that has been considered is depicted in Fig. 4. A 100 m deep and 100 m long horizontal fracture is bounded by two impervious blocks. A 500 kPa injection pressure Δp_{inj} is applied to one extremity, and the fracture is bounded by a high permeability region, where the initial pressure p_{ini} is kept constant, at the other extremity. The model assumes plane flow and plane strain conditions. The parameters of the model are listed in Table 1. Moreover, a unit coupling factor f_c is assumed, which implies $e = e_h = \bar{e}$, and, as previously mentioned, T_f is evaluated by means of the cubic law. A sensitivity analysis is performed with the normal stiffness k_{nn} having the following values: 0.1, 1, 10, 100 GPa/m. All the segments that define the boundary are divided into 5 elements, including the fracture.

The length of each element of the fracture is 20 m; this value obviously exceeds any plausible value of the spatial correlation length l_c. When dealing with large-scale problems, the use of elements, whose length is several orders of mag-

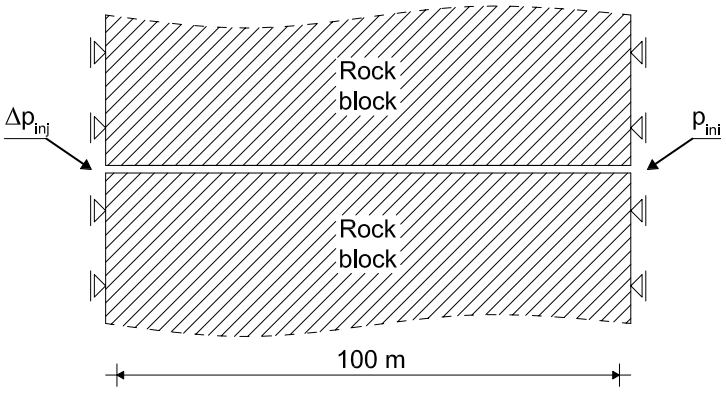

Fig. 4. Scheme of the model used in injection test simulation

Table 1. Material properties introduced into the model

Rock	
Density ρ_r	$2500\,\mathrm{kg/m^3}$
Young modulus E_r	$10 \div 100\,\mathrm{GPa}$
Poisson ratio ν_r	0.25
Fracture	
Normal stiffness k_{nn}	$0.1 \div 100\,\mathrm{GPa}$
Tangential stiffness k_{tt}	$0.5\,\mathrm{GPa/m}$
Initial aperture e	$10^{-4}\,\mathrm{m}$
Fluid	
Density ρ_w	$1000\,\mathrm{kg/m^3}$
Compressibility β_w	$5 \cdot 10^{-1}\,\mathrm{GPa^{-1}}$

nitude smaller than a characteristic length of the problem, is not practicable. If the single fracture element is viewed as a series of resistors of length l_c, an equivalent transmissivity can be calculated, provided the portion along which this calculation is performed is subject to a uniform pressure gradient. As a consequence, in a problem where high gradients are expected, the length of these *equivalent* elements should be tailored to the distribution of the gradients (i.e. to follow a rapid variation, a fine discretization should be considered). A coarse discretization was selected for the subsequent numerical experiments to reduce the computation time, irrespective of the previously mentioned considerations. The definition of a criterion for the length of the equivalent element is not the purpose of this work.

It is worthwhile mentioning that the k_{nn} values selected for the sensitivity analysis refer to different tendencies of the fracture to modify its transmissivity when it undergoes deformation, which also depends on the stiffness of the rock blocks, geometry and boundary conditions. All these factors together control the fracture *deformability* which, in a loose sense, is herein used as a substitute for the overall system deformability.

The results of the numerical experiments clearly show the importance of the indirect coupling; a great increase in transmissivity can occur during an injection which in turn affects the fluid flow regime and the evolution of fluid pressure. This modification can in part be permanent if hysteretical behaviour of the fracture subsists.

4.1 Results for Constant Stiffness

The results are illustrated in terms of flow rate at the injection point and pressure and transmissivity variations along the fracture. The flow rates Q_{inj} at the injection point and for $E_r = 10\,\text{GPa}$ are shown in Fig. 5 in detail. For k_{nn} equal to 10 and 100 GPa/m, the Q_{inj} values plot as a typical decreasing curve of the diffusion equation. For the lower k_{nn} values, the solution shows a peak followed by the post-peak phase whose temporal extension increases with the stiffness. This response is induced by the dramatic increase in transmissivity near the injection point. At the beginning, the fracture is propped open by the pressure and the flow rate rapidly increases as a consequence of the quick increase in transmissivity. The subsequent reduction in the pressure gradients reverses this tendency. Nevertheless, the steady-state flow rate is consistently higher than for the higher k_{nn} values.

The Q_{inj} values are plotted versus time in Fig. 6 for k_{nn} equal to 1 GPa/m in conjunction with E_r equal to 1, 10 and 100 GPa. It is apparent from this figure that, even for a very low fracture stiffness, the bell-shaped curve is not reproduced when the stiffness of the rock increases.

The values of transmissivity T_f and pressure p along the fracture are plotted in Figs. 7 and 8 for a rather deformable fracture ($k_{nn} = 0.1\,\text{GPa/m}$). With the progressive

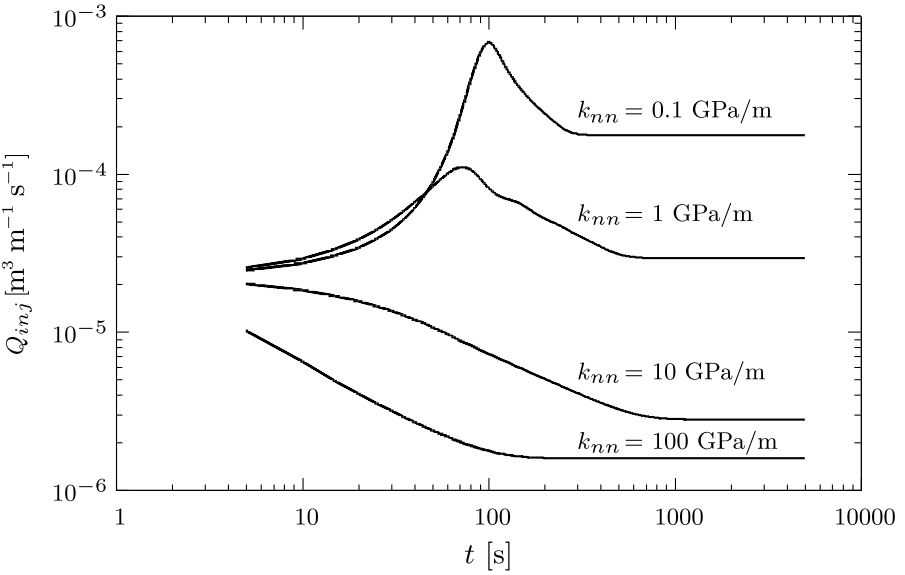

Fig. 5. Flow rate Q_{inj} at the injection point versus time t ($k_{nn} = 0.1 \div 100\,\text{GPa/m}$, $E_r = 10\,\text{GPa}$)

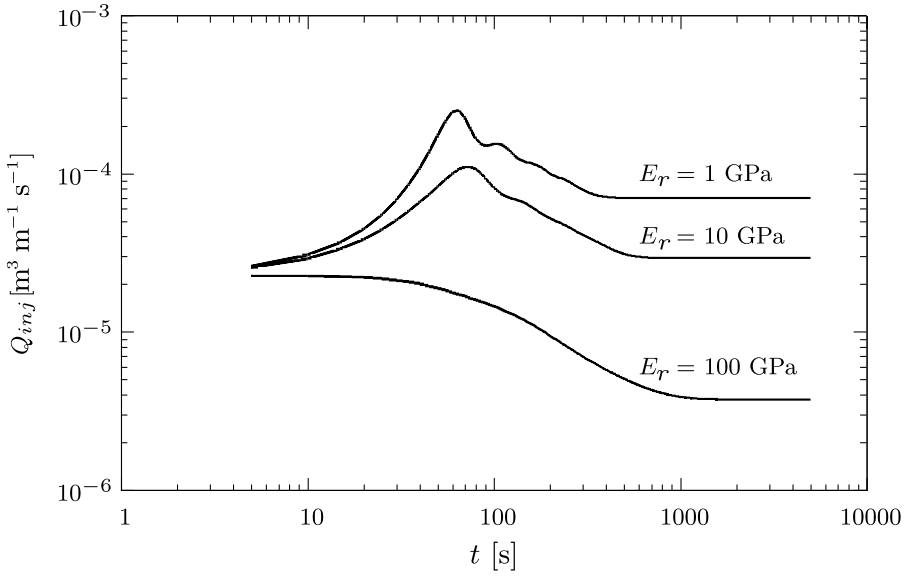

Fig. 6. Flow rate Q_{inj} at the injection point versus time t ($k_{nn} = 0.1$ GPa/m, $E_r = 1$, 10, 100 GPa)

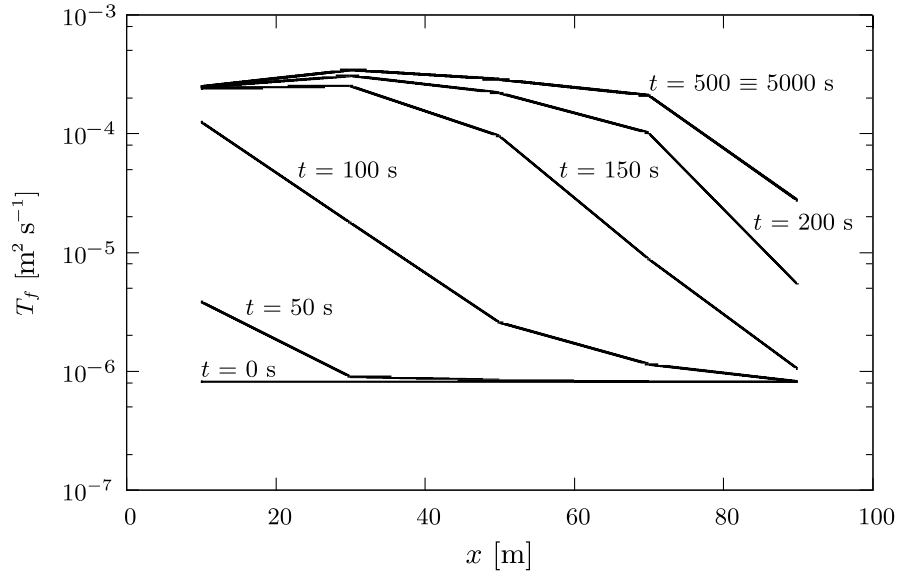

Fig. 7. Values of transmissivity along the fracture for different t values ($k_{nn} = 0.1$ GPa/m, $E_r = 10$ GPa)

opening of the fracture, the transmissivity in the far-field increases up to the final value which is reached after about 500 seconds. Near the injection point, the final value is reached after 100 seconds (Fig. 7). Afterwards, the increase in transmissivity also propagates to the far-field. In the last phase (200 seconds), the flow rate Q_{inj} decreases

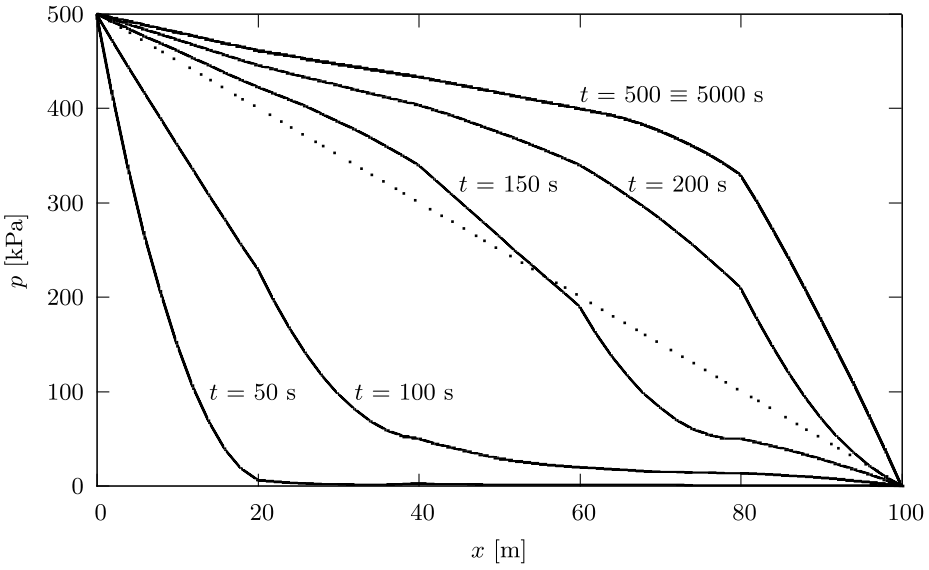

Fig. 8. Values of pressure along the fracture for different t values ($k_{nn} = 0.1\,\text{GPa/m}$, $E_r = 10\,\text{GPa}$). The dashed line represents the steady-state values for a pure hydrogeological solution

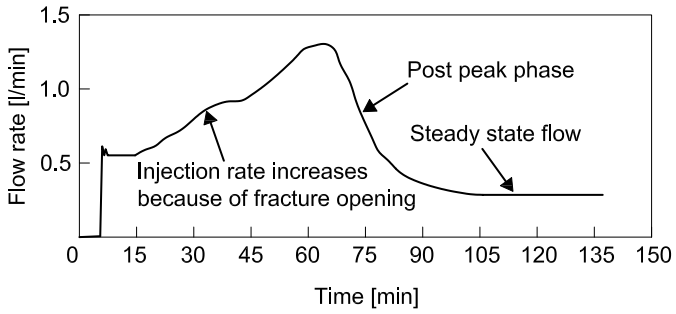

Fig. 9. Flow rate response during a constant pressure injection into a subhorizontal fracture (after Alm, 1999)

because the maximum deformation of the fracture is reached and the pressure gradients are reduced, as previously mentioned. This behaviour has also been experimentally obtained by Alm (1999) (Fig. 9). Finally, the long-term pressure distribution does not conform to the classical linear steady-state hydrogeological solution, which considers constant T_f throughout the process, as shown by the dashed line in Fig. 8 and this fact constitutes one of the main reasons for the use of a HM coupling model.

4.2 Results for Stress-dependent Stiffness

The HM coupled response for the problem of Fig. 4 was tested under injection by setting a stress-dependent stiffness to the fracture. The Saeb and Amadei (1992) model – modified by Souley et al. (1995) – was considered for the simulation

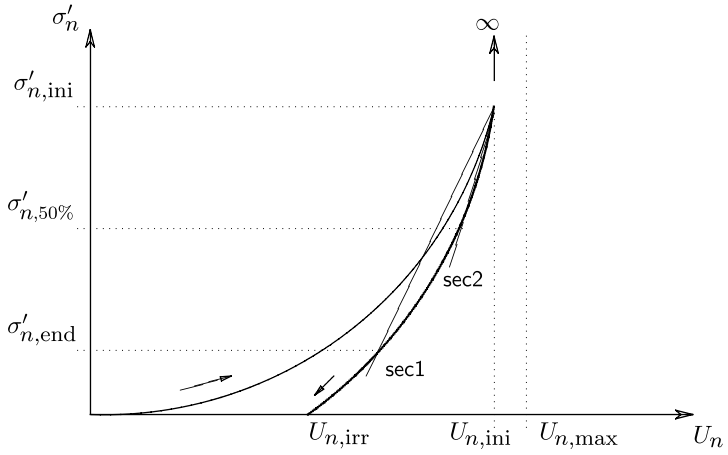

Fig. 10. Extended version of the Saeb and Amadei model

(Fig. 10). This model can be envisaged as a generalization of the models introduced earlier by Goodman (1976) and Bandis et al. (1983).

The injection test curve is hyperbolic with asymptot for $U_n = U_{n,\max}$. The irrecoverable normal displacement $U_{n,\mathrm{irr}}$ is also required when unloading is completed. This parameter depends on the maximum level of normal stress $\sigma'_{n,\mathrm{ini}}$ prior to unloading for the given loading (L)-unloading (U) cycle. As assumed in the model, the initial normal stiffness for unloading $k_{nn,\tan,0(\mathrm{U})}$ (defined at ($U_{n,\mathrm{irr}}$, 0)) is equal to the secant to the loading curve at the point ($U_{n,\mathrm{ini}}$, $\sigma'_{n,\mathrm{ini}}$):

$$k_{nn,\tan,0(\mathrm{U})} = \frac{\sigma'_{n,\mathrm{ini}}}{U_{n,\mathrm{ini}}}. \tag{48}$$

The normal stiffness k_{nn} of the fracture has the following expression:

$$k_{nn} = k_{nn,\tan,0(\mathrm{U})}\left(1 - \frac{\sigma'_n}{k_{nn,\tan,0(\mathrm{U})}(U_{n,\max} - U_{n,\mathrm{irr}}) + \sigma'_n}\right)^{-2}. \tag{49}$$

An initial effective stress $\sigma'_{n,\mathrm{ini}}$ of 700 kPa was considered in the example. Three different injection pressure Δp_{inj} levels were applied, corresponding to the 85%, 70% and 60% of $\sigma'_{n,\mathrm{ini}}$, while the final effective stress at the injection point $\sigma'_{n,\mathrm{end}}$ had values of 100, 200 and 300 kPa respectively. The iterative procedure for the computation of the stiffness begins by assuming, as a first trial, k_{nn} equal to the value that corresponds to the tangent stiffness at point ($U_{n,\mathrm{ini}}$, $\sigma'_{n,\mathrm{ini}}$) of the injection test curve, when unloading begins, then the value is adjusted using the slope of the secant. The parameters used for this test are $k_{nn,\tan,0(\mathrm{L})} = 0.1\,\mathrm{GPa/m}$, $k_{nn,\tan,0(\mathrm{U})} = 7.1\,\mathrm{GPa/m}$, $U_{n,\mathrm{irr}} = 8.7 \cdot 10^{-5}\,\mathrm{m}$, $U_{n,\max} = 1 \cdot 10^{-4}\,\mathrm{m}$.

The flow rate is shown in Figs. 11, 12 and 13, where the comparisons are given with the results of the simulation for a normal constant stiffness k_{nn} equal to $k_{nn,\mathrm{sec1}}$; this latter value (`sec1` in Fig. 10) is equal to the slope of the secant drawn between $\sigma'_{n,\mathrm{ini}}$ and $\sigma'_{n,\mathrm{end}}$. In all cases, the flow rate Q_{inj} predicted by the constant k_{nn} model is slightly different from the Q_{inj} given by the stress-dependent k_{nn} model. The difference

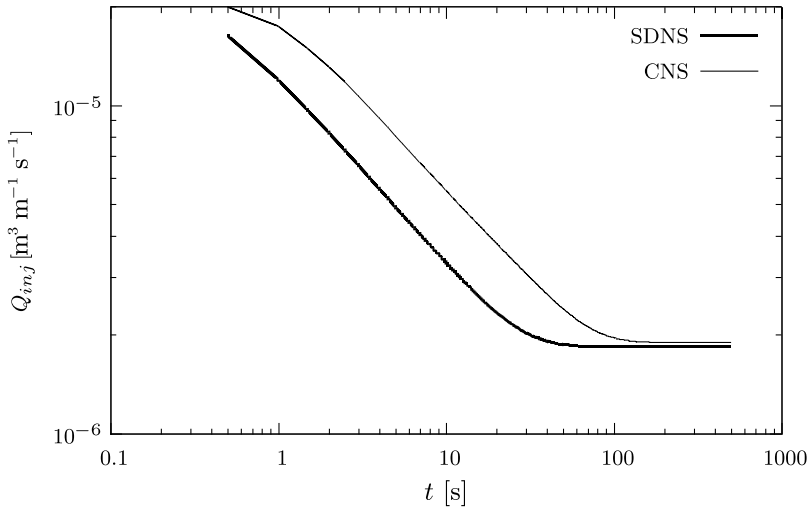

Fig. 11. Flow rate Q_{inj} versus time t: comparison between the model with stress-dependent (SDNS) and constant (CNS) k_{nn} for $\Delta p_{\text{inj}} = 85\%\sigma'_{n,\text{ini}}$

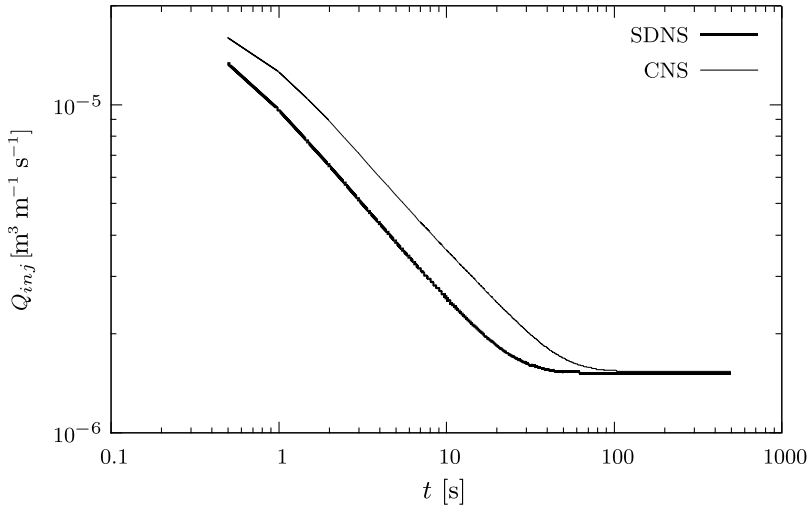

Fig. 12. Flow rate Q_{inj} versus time t: comparison between the model with stress-dependent (SDNS) and constant (CNS) k_{nn} for $\Delta p_{\text{inj}} = 70\%\sigma'_{n,\text{ini}}$

reduces for smaller values of the injection pressure. However, the steady-state values are the same.

Further simulations where therefore performed for the case with $\Delta p_{\text{inj}} = 70\%\sigma'_{n,\text{ini}}$, with higher values of $k_{nn,\text{sec}}$, with the aim of finding a better match with the results of the non-linear model. In this specific case, a perfect match is given for k_{nn} equal to $k_{nn,\text{sec2}}$, corresponding to the secant (`sec2` in Fig. 10) drawn between $\sigma'_{n,\text{ini}}$ and $\sigma'_{n,50\%} = 450\,\text{kPa}$ (Fig. 14). It is clear that the use of a stress-dependent stiffness is

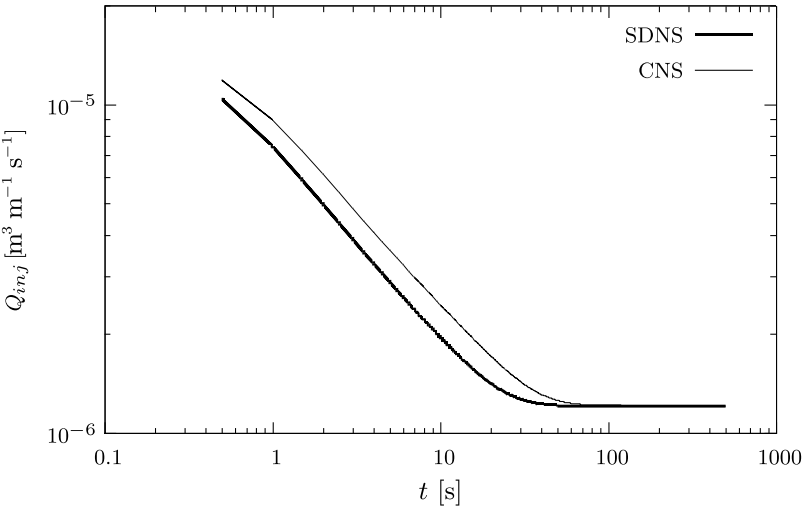

Fig. 13. Flow rate Q_{inj} versus time t: comparison between the model with stress-dependent (SDNS) and constant (CNS) k_{nn} for $\Delta p_{\text{inj}} = 60\%\sigma'_{n,\text{ini}}$

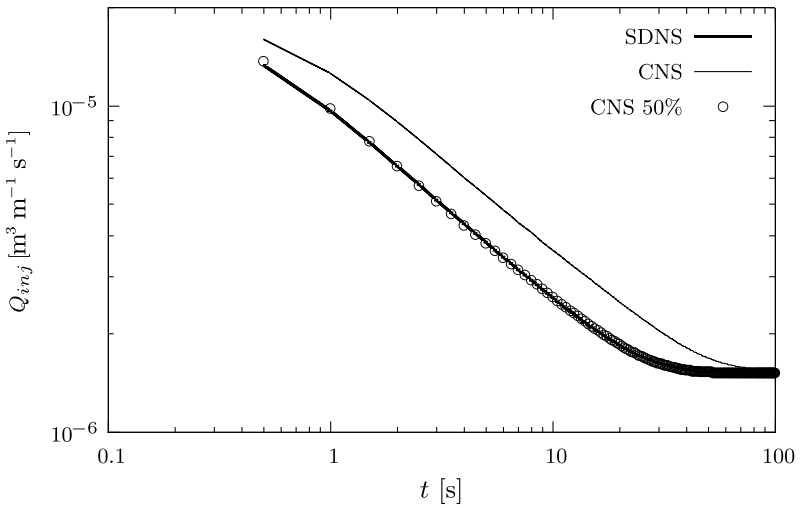

Fig. 14. Flow rate Q_{inj} versus time t: comparison between the model with stress-dependent k_{nn} (SDNS) and with two constant values for k_{nn} (CNS, CNS 50%)

not advantageous when dealing with injection problems, given the particular shape of the unloading curve of the non-linear model adopted.

5. Conclusions

The hydro-mechanically coupled response of a rock fracture in an injection test has been assessed through a BEM-FEM code which analyses an assembly made of impervious elastic blocks intersected by percolative deformable fractures. Emphasis was

placed on the implications in the fluid flow regime and system deformation when HM coupling is dominant. Several analyses were carried out from which the following statements can be drawn:

– The most relevant implication of HM coupling, during an injection test, is the great variation in transmissivity that can occur in the near-field of a deformable fracture (close to the injection point) as a consequence of the induced opening. This variation is locally distributed and the discretization of the fracture is consequently required to follow this variation.

– Systematic modelling, using a non-linear stress-closure relation and stress-dependent stiffness, does not appear to be justified with respect to the HM response of a fracture during an injection test. Because of the particular conditions of the example, the flow rate computed with the non-linear model can also be obtained using an appropriate constant value of k_{nn}. In principle, this would suggest removing an unnecessary source of complexity from the computational scheme through the use of a suitable constant fracture stiffness model.

Acknowledgements

The authors wish to thank the Italian ENEL Ricerca SpA for a first funding provided for the development of the code and the Swiss Hauptabteilung für die Sicherheit der Kernanlagen (HSK) for the current funding in the framework of the ETH-HSK Radioactive Waste Disposal Research Collaboration. Dr. Fidelibus would also like to thank Prof. Simon Löw of the ETH for the constant support given during the development of the code. The Politecnico di Torino and its Doctoral School should also be thanked for providing support for Dr. Cammarata during his stay at ETH.

References

Alm, P. (1999): Hydromechanical behaviour of a pressurized single fracture: an in situ experiment. PhD Thesis, Chalmers University of Technology, Göteborg, Sweden.

Bandis, S., Lumsden, A., Barton, N. (1983): Fundamentals of rock joint deformation. Int. J. Rock Mech. Min. Sci. Geomech. Abstr. 20(6), 249–268.

Bear, J. (1979): Hydraulics of groundwater. McGraw-Hill, New York.

Bear, J., Bachmat, Y. (1990): Introduction to modeling of transport phenomena in porous media. Kluwer Academic Publisher, Dordrecht.

Becker, A. (1992): Boundary element method in engineering. McGraw-Hill, Maidenhead.

Brebbia, C., Telles, J., Wrobel, L. (1984): Boundary element techniques. Springer-Verlag, Berlin Heidelberg New York Tokyo.

Cornet, F., Li, L., Hulin, J., Ippolito, I., Kurowski, P. (2003): The hydromechanical behaviour of a fracture: an in situ experimental case study. Int. J. Rock Mech. Min. Sci. 40, 1257–1270.

Fidelibus, C. (2003): A code for the hydro-mechanical response of an assembly of rock blocks and discrete fractures. Tech. Rep. ETH Report 3465/29, ETH, Zürich, Switzerland.

Fidelibus, C., Barla, G., Cravero, M. (1997): A mixed solution for two-dimensional unsteady flow in fractured porous media. Int. J. Numer. Anal. Methods Geomech. 21, 619–633.

Goodman, R. (1976): Methods of geological engineering in discontinuous rock. West Publishing, New York.

Hakami, E. (1995): Aperture distribution of rock fractures. PhD Thesis, Royal Institute of Technology, Stockholm, Sweden.

Huyakorn, P., Pinder, G. (1983): Computational methods in subsurface flow. Academic Press, New York.

McDermott, C. I., Kolditz, O. (2004): Hydraulic-geomechanical effective stress model: determination of discrete fracture network parameters from a pump test and application to geothermal reservoir modelling. In: Proc. 29th Workshop on Geothermal Reservoir Engineering, Stanford, California, pp SGP-TR-175.

Saeb, S., Amadei, B. (1992): Modelling rock joints under shear and normal loading. Int. J. Rock Mech. Min. Sci. Geomech. Abstr. 29(3), 267–278.

Souley, M., Homand, F., Amadei, B. (1995): An extension to the Saeb and Amadei constitutive model for rock joints to include cyclic loading paths. Int. J. Rock Mech. Min. Sci. Geomech. Abstr. 32(2), 101–109.

Wang, H. (2000): Theory of linear poroelasticity. Princeton University Press, Princeton.

Yeo, I., De Freitas, M. D., Zimmerman, R. (1998): Effect of shear displacement on the aperture and permeability of a rock fracture. Int. J. Rock Mech. Min. Sci. 35(8), 1051–1070.

Zimmerman, R., Bodvarsson, G. (1996): Hydraulic conductivity of rock fractures. Transp. Porous Media 23, 1–30.

Authors' address: Dr. Giuseppe Cammarata, Dipartimento di Ingegneria Strutturale e Geotecnica, Politecnico di Torino, c.so Duca degli Abruzzi 24, 10129 Torino, Italy; e-mail: giuseppe.cammarata@polito.it